This article has been accepted for inclusion in a future issue of this journal. Content is final as presented, with the exception of pagination.

Control Co-Design of Hydrokinetic Turbines Considering Dynamic–Hydrodynamic Coupling

Boxi Jiang, Mohammad Reza Amini, Yingqian Liao, Kartik Naik, Joaquim R. R. A. Martins, and Jing Sun, *Fellow, IEEE*

***Abstract*— Hydrokinetic turbine (HKT) controllers are traditionally optimized after determining physical turbine variables. However, simultaneously varying controls and turbine shape by considering the interactions between the control space and the turbine shape can significantly enhance the system performance in contrast to the conventional sequential design approach. This article delves into this prospect by introducing a control co-design (CCD) framework tailored for this simultaneous optimization for a variable-speed HKT rotor. The proposed CCD framework integrates a dynamic–hydrodynamic model that captures the intricate interplay between hydrodynamic performance and control strategies for the HKT under time-varying flow profiles. We systematically investigate cases with diverse control constraints in a time-varying flow environment to explore the coupling between the control space and the physical system. We demonstrate the advantages of the CCD framework over the conventional sequential design methodology through comparative study cases. CCD optimization considering a single flow condition leads to an overly specialized design that underperforms at other off-design conditions. The stochastic nature of the flow thereby highlights the need to account for a broader range of flow speeds in the HKT design process. To address this challenge, we introduce a multipoint CCD optimization that accounts for the annual flow probability distribution. The multipoint CCD approach demonstrates higher annual energy extraction compared to optimizations based on a single flow condition.**

***Index Terms*— Co-design, control co-design (CCD), hydrokinetic turbines (HKTs), water current energy.**

NOMENCLATURE

η	System efficiency.
λ	Tip speed ratio.
ω	Turbine angular speed.
ρ	Density of water.
θ	Twist angles.
c	Chord lengths.
C_P	Power coefficient.
$E_{r,\theta}$	Relative variance in twist angles.
$E_{r,c}$	Relative variance in chord lengths.
i	ith element of the turbine blade.
I_{HKT}	Turbine inertia.
$p(v_k)$	Probability density of the kth flow condition.
Q	Flow-induced torque.
r	Radius of a turbine.
t	Time.
u	Control variable.
$u_{\max}$	Upper bound of the control variable.
v	Flow velocity.
AEP	Annual energy production.
BEM	Blade element momentum.
CCD	Control co-design.
HKT	Hydrokinetic turbine.
LCoE	Levelized cost of energy.
MHK	Marine hydrokinetic.

Manuscript received 20 May 2024; revised 5 July 2024; accepted 21 July 2024. This work was supported by the United States Department of Energy (DOE)-Advanced Research Projects Agency-Energy (ARPA-E) through the Submarine Hydrokinetic and Riverine Kilo-Megawatt Systems (SHARKS) Program under Award DE-AR0001438. Recommended by Associate Editor K. Worthmann. *(Corresponding author: Jing Sun.)*

Boxi Jiang, Mohammad Reza Amini, Kartik Naik, and Jing Sun are with the Department of Naval Architecture and Marine Engineering, University of Michigan, Ann Arbor, MI 48109 USA (e-mail: boxij@umich.edu; mamini@umich.edu; naikk@umich.edu; jingsun@umich.edu).

Yingqian Liao was with the Department of Aerospace Engineering, University of Michigan, Ann Arbor, MI 48109 USA. She is now with the National Renewable Energy Laboratory, Golden, CO 80401 USA (e-mail: yqliao@umich.edu).

Joaquim R. R. A. Martins was with the Department of Aerospace Engineering, University of Michigan, Ann Arbor, MI 48109 USA (e-mail: jrram@umich.edu).

Digital Object Identifier 10.1109/TCST.2024.3440249

I. INTRODUCTION

RENEWABLE energy has become increasingly important to meeting the growing energy demands. Among all the forms of renewable energy, MHK energy has been recognized as a promising one due to its availability, predictability, and high energy density. Recent studies suggest that around 50 GW of power can be produced from tidal currents in USA [1], [2], plus an additional 32-GW power available from rivers [3] and offshore ocean currents [4]. The power density of the current MHK with 1.6-m/s flow speed can reach up to 2 kW/m^2, much higher than that of wind and solar power.

Among all hydrokinetic energy systems, HKTs attract significant research attention. Myers and Bahaj [5] measured the hydrodynamic forces for an HKT with 0.4 m radius in a towing tank. The maximum power coefficient reached 0.45. Chen et al. [6] tested the performance of a ducted turbine in a marine-current environment and designed a tidal current energy capture system with a floating platform. Thurlbeck and Cao [7] developed a condition monitoring system that provides maintenance guidance in harsh underwater environments. Marine Current Turbines Ltd. [8] deployed HKT systems of 1-MW power level for long-term operation.

Despite the extensive research efforts in the field, HKTs are still not practical renewable energy sources, as no large-scale HKT farm exists as of now. This reality can be attributed

1063-6536 © 2024 IEEE. Personal use is permitted, but republication/redistribution requires IEEE permission.
See https://www.ieee.org/publications/rights/index.html for more information.

Authorized licensed use limited to: University of Michigan Library. Downloaded on August 20,2024 at 02:29:56 UTC from IEEE Xplore. Restrictions apply.

This article has been accepted for inclusion in a future issue of this journal. Content is final as presented, with the exception of pagination.

to multiple reasons, including harsh environment and costly electricity transmissions [9]. Among them is the power efficiency degradation when operating in a time-varying flow condition. While HKT systems are highly multidisciplinary, the design of an HKT is often performed sequentially. The traditional design-then-control (sequential) approach focuses on steady-state power efficiency during the design phase, making it a challenge for control to track the maximum power point in a time-varying flow condition. The initial phase of exploration involves examining the rotor's physical design variables. Although the phase considers the coupling between the hydrodynamic and structural strength, it does not consider control and focus on the steady-state performance of the system [10]. Once the physical design is determined, the control design is conducted to optimize the transient performance of the system [11]. In highly dynamic and interactive systems such as HKT, the sequential design method fails to capitalize on the synergy between the physical components and the control system dynamics. This often leads to less-than-optimal designs or excessively restrictive control solutions.

Alternatively, the physical and control systems can be designed in an integrated manner to mitigate the limitations of the sequential design. This integrated multidisciplinary design optimization (MDO) approach is referred to as control co-design (CCD). The approach of CCD entails the concurrent development of both system design and control variables and offers advantages to renewable energy devices operating in time-varying environments. Hence, this approach achieves the optimal system-level performance and better tradeoff management [12]. Multiple examples have shown the benefits of such an approach to engineering problems [13], [14].

Recent CCD studies in the context of renewable energy systems have demonstrated notable advancements in enhancing power production and reducing associated costs. Regarding offshore wind turbines (OWTs), Deshmukh and Allison [15] introduced a design methodology that integrates structural and control system elements. Their approach, illustrated through various case studies, showed substantial performance enhancements compared to traditional sequential design methods. Pao et al. [16] developed a co-design process considering subsystems, including aerodynamics, structures, and control. The work leads to a 25% reduction in the LCoE for a 13-MW wind turbine compared to the baseline three-bladed upwind rotor. In the field of hydrokinetic energy devices, Naik et al. [17] developed a CCD methodology to design a hydro-energy kite. Coe et al. [18] conducted a conceptual demonstration of CCD for a wave energy converter (WEC). O'Sullivan and Lightbody [19] presented a CCD formulation to optimize a complete wave-to-wire system.

While previous works on CCD for other renewable energy structures provide valuable insights, the tools and results cannot be directly applied to HKTs due to significant differences in their structures, hydrodynamic responses, and design constraints. For instance, HKTs operate in harsh underwater environments and typically do not have variable pitch control [6], which is a common feature in large OWTs. Also, some HKTs consider a direct-drive configuration [20], which connects the rotor directly to the generator without gearboxes. While the direct-drive configuration has merits such as fewer moving parts, lower maintenance, and higher reliability, it also brings some challenges in terms of limited control authorities. These unique characteristics highlight the need for a tailored CCD framework for the HKTs, which, however, has not been fully explored. While Hasankhani et al. [2] optimized a buoyancy-controlled HKT with a nested CCD framework, the research tackled a significantly different turbine system (variable buoyancy) with the control objective being path planning in a spatiotemporal flow. It remains an open topic to explore the coupling between the HKT rotor design (defined by discretized chord and twist profiles) and the control (defined as generator load) for maximum power generation. Our previous work presents a CCD formulation for HKT and cases where CCD outperforms the sequential method [21]. However, the design flow condition dictates the physical designs. This dependence leads to practical issues because the design needs to operate in complex realistic conditions.

This article presents a CCD framework tailored for optimizing the rotor design in HKT. It employs a model that integrates both dynamics and hydrodynamics within the CCD context, aiming to maximize energy production across various time-varying flow profiles. We consider twist angles and chord lengths defined at discretized rotor blade sections as the physical design variables (see Fig. 1). The strategy of open-loop optimal torque control is implemented to achieve the highest power production from the HKT. This article details and analyzes aspects such as the physical designs, state and control trajectories, and power production outcomes. The geometries and power outputs of CCD designs are evaluated in comparison to those from sequential designs, under identical flow profiles and control constraints. Findings indicate that CCD approaches yield greater energy production when control constraints are present, surpassing the performance of the traditional sequential (design-then-control) methodology. Given that the flow velocity varies over a given year, a multipoint CCD framework is developed based on the velocity probability distribution, leading to a more efficient design with improved annual energy production (AEP).

The contributions are threefold. First, CCD frameworks, both single point and multipoint, are formulated for an HKT employing open-loop optimal torque control. Second, compared with a sequential design, a comprehensive performance evaluation of the CCD results is carried out to reveal dynamic–hydrodynamic interactions. Third, a multipoint CCD is conducted to yield a more energy-efficient design based on flow probability density for AEP maximization.

The rest of this article is presented as follows. Section II introduces the problem formulations, including the design objectives, control method, design variables, and assumptions used in this study. Section III provides the hydrodynamic and dynamic models along with the validations. Section IV presents the CCD formulation for HKTs. Section V discusses the single-point CCD results and the comparison with sequential designs. Section VI presents a multipoint CCD for maximum AEP. Finally, Section VII summarizes the main contributions with conclusions.

Authorized licensed use limited to: University of Michigan Library. Downloaded on August 20,2024 at 02:29:56 UTC from IEEE Xplore. Restrictions apply.

This article has been accepted for inclusion in a future issue of this journal. Content is final as presented, with the exception of pagination.

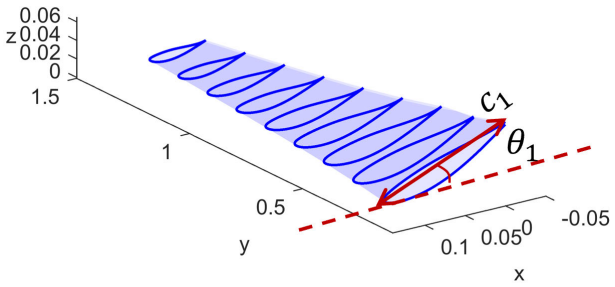

Fig. 1. Blade geometry shows the physical design variables: twist angles θ and chord lengths c for each element. The foil elements of the blade are illustrated with solid lines. The negative x-direction is the anticipated flow direction, and the y-direction is along the turbine radius. θ is the angle between chord lengths and the xy plane.

TABLE I

PARAMETERS OF BAHAJ'S HKT AND THE 5-kW BASELINE MODEL, WHICH IS SCALED UP FROM BAHAJ'S HKT USING A FACTOR OF 3.5

	Bahaj HKT [22]	**Model**
Rated power (kW)	0.4	5.0
Rated flow speed (m/s)	1.7*	1.7
Rotor radius (m)	0.4	1.4
Reynolds number (–)	2×10^5	8×10^5
Number of blades (–)	3	3

* Maximum towing speed in the tests [22].

II. HKT OPTIMIZATION FORMULATION

In this section, we introduce the design optimization framework of HKT. The objective of this study is to maximize the energy production of an HKT with a time-varying flow condition through rotor physical design and control. The turbine considered is a direct-drive variable-speed fixed-pitch turbine and targets a 5-kW rated power for microgrid applications. Control authority is limited for such a system. The baseline is a three-bladed horizontal axis HKT. The rotor blade of an HKT was divided into different elements, as shown in Fig. 1. The baseline model, control method, and design variables are introduced in the following.

A. Baseline HKT Design

The baseline model is adopted from [22], for the HKT developed and tested by Bahaj et al. [22]. The model is scaled with a factor of 3.5:1 to have 5-kW rated power for microgrid applications in remote areas [23]. The geometric scaling is applied by linearly scaling the character length, including the turbine radius and chord length distributions. The twist angle distributions remain the same as defined by Bahaj et al. [22]. As a simplification, the model uses the same NACA63815 profile along the radius for its foil geometry. Table I lists the parameters for both Bahaj's turbine and the baseline HKT model, including details such as dimensions and performance characteristics. The Reynolds number is estimated by the relative speed of the turbine blade at 70% foil span. As the Reynolds number of the baseline turbine with 1.4 m diameter is different from the reference turbine with 0.4 m diameter, the foil drag polar and the power coefficient are recalculated and compared to the reference turbine in Section III-A.

B. Open-Loop Optimal Control

Because the flow speed is time-varying, control is needed for a variable-speed HKT to operate at its maximum power point [24], defined by the physical design. In this article, we focus on the best achievable performance (ceiling performance) in CCD and choose open-loop optimal torque control. The control optimizes the generator torque time profile to maximize the power generation based on the given flow speed. Open-loop control trajectory optimization assumes full knowledge of the system without uncertainty and the environment and represents the best possible performance. The control authority is limited due to physical and operational constraints. In Section V, we will present different scenarios that activate the constraint on control load. Such a control assumes that the inflow velocity is measured with sensors. The design of real-time control is the step after the CCD to address the time delays, feedback, sensor noise, and so on.

It should be noted the open-loop optimal control delineated in this article is used to demonstrate performance potential for the ideal case with full knowledge of flow speed and is not practical for real-world applications. For practical applications, feedback controls are more suitable for maximum power tracking in the presence of disturbances and flow uncertainties. CCD can also be performed within the closed-loop framework, as shown in [25] and [26].

C. Design Variables

As shown in Fig. 1, the physical design variables consist of the chord lengths c_i $(i = 1, 2, \ldots, N)$ and twist angles θ_i $(i = 1, 2, \ldots, N)$, for the N segments in the HKT discretization. According to Chica et al. [27], these physical design variables are the key design variables for HKT rotor design and have a significant influence on power production. In this study, we use $N = 9$. The 9th segment is taken at the edge of the blade and other sections are linearly distributed in the middle of the blade with a step of 0.14 m, which is 10% of the HKT radius. The turbine radius, the number of blades, and the foil geometry are fixed to the baseline values in the optimization.

D. Design Assumptions

The assumptions made for the hydrodynamics, dynamics, and control of the HKT system are summarized as follows.

First, the hydrodynamics are calculated with a constant Reynolds number during the CCD optimization. Assumptions are made that the power coefficient of the hydrofoil is not sensitive to the Reynolds number within the range of operation. The changes in flow velocity and c in the optimization influence the Reynolds number and thus hydrodynamics. As for a 1.4-m HKT studied in this work, the Reynolds number is around 8×10^5. Within such a range, the influence of the Reynolds number on the power coefficient of the rotor is minor as long as the change in Reynolds number is small, according to the experiment results on a small-scale propeller [28]. However, such a minor effect can be computationally expensive to capture in optimization due to its nonlinear characteristics.

Authorized licensed use limited to: University of Michigan Library. Downloaded on August 20,2024 at 02:29:56 UTC from IEEE Xplore. Restrictions apply.

This article has been accepted for inclusion in a future issue of this journal. Content is final as presented, with the exception of pagination.

Second, the dynamic model is simplified by assuming a rigid drive train. The assumption is valid and generally applied in the modeling of a direct-drive turbine.

Third, the flow velocity and turbine rotational speed are assumed to be measured with sensors. Such an assumption is needed for the implementation of the open-loop optimal control. This assumption can be relaxed with flow estimation algorithms [29].

III. Modeling and Validation

The CCD of an HKT simultaneously solves for the optimal control trajectory, the HKT's states, such as the rotating speed, and the corresponding flow-induced torque, which are determined by physical design variables. In this article, the hydrodynamics of HKTs are computed using the BEM [30] theory. The details are introduced in Section III-A.

The dynamic model is simplified by assuming a rigid drivetrain. Details are introduced in Section III-B.

Section III-C introduces the optimizer. We implement the model in OpenMDAO, leveraging its modular approaches and coupled derivative computation for system analysis and optimization [31]. We use analytical derivatives for each component. Using analytical derivatives and the coupled adjoint method with gradient-based optimization enables efficient and scalable design optimizations with many design variables.

A. Hydrodynamic Modeling and Tool Validation

In this study, the hydrodynamics of HKTs is modeled in a quasi-static way. The power coefficient (C_P) is computed for varying tip speed ratio (λ) using the BEM-based CCBlade [32] package. The lift-drag coefficient polar data were computed with XFOIL [33]. First, to validate the hydrodynamic tools, we computed the lift-drag coefficient polar data and C_P at a Reynolds number of 2×10^5 for a 0.4-m HKT, which is the same scale as in the tank test by Bahaj et al. [22]. Then, we recomputed the polar data for the 1.4-m scaled model with a Reynolds number of 8×10^5. The flow transition was forced at 2% of the chord for all angles of attack. The polar data are then combined with the momentum theory to predict the performance of the entire turbine. The flow-induced torque (Q) and power (P) are calculated based on the polar data, the chord length, the flow speed, and the turbine rotational velocity with BEM. The power performance can be characterized further by the relationship of the nondimensional parameters C_P and λ. As shown in Fig. 2, the C_P curves predicted from CCBlade capture the trend and range reasonably well compared to the experimental result, with the root-mean-square error being 0.013.

To validate the capability of instantaneous quasi-static hydrodynamic modeling to capture system dynamics and predict energy extraction, the quasi-static BEM modeling was also compared with a dynamic inflow modeling by Henriksen et al. [34]. In contrast to quasi-static modeling where the axial induced flow velocity v_n settles instantly to the steady-state value, dynamic inflow modeling considers the temporal development of v_n using the first-order filter, which more accurately captures the wake effect in a time-varying flow.

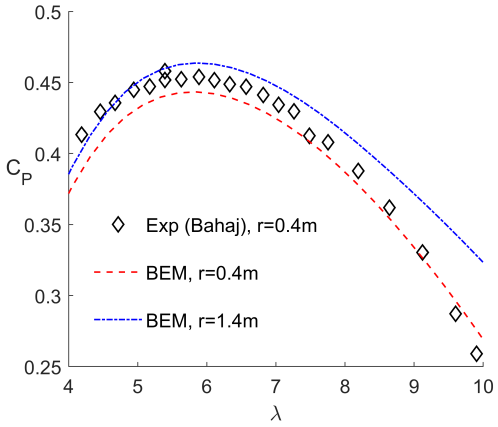

Fig. 2. Comparisons of C_P between BEM results and Bahaj's tank test results. The BEM result for the 0.4-m-radius (r) HKT is calculated with a Reynolds number of 2×10^5, while the 1.4-m-radius HKT is calculated with a Reynolds number of 8×10^5.

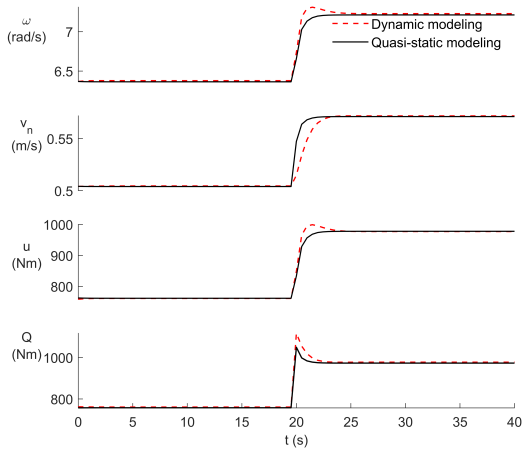

Fig. 3. Comparisons on turbine rotating speed, induced velocity, control trajectory, and fluid-induced torque between quasi-static and dynamic inflow modeling. Both models converge to the same steady-state performance and the difference in energy production is 1.1%.

The turbine performance with these two different flow modelings is compared at a step inflow condition, which is defined as $v = 1.5 + 0.2H(t - 20)$ m/s, where $H(t)$ is the Heaviside step function. Due to the numerical difficulty in finding the optimal control trajectory in such extreme, nonsmooth inflow conditions, a quadratic ("$k\omega^2$") feedback control [35] is applied here only for model validation purposes. The results are shown in Fig. 3. As expected, both models converge to the same steady-state performance. Also, because the modeling of induced velocity differed when the flow velocity changed, the angle of attack was different between the two models. However, such a difference leads to minor changes in the rotating speed ω and the flow-induced torque Q. Consequently, the predicted energy production difference between the quasi-static and dynamic inflow model is 1.1% for a 40-s simulation. Due to the minor difference in the power generation and the control trajectories, the quasi-static hydrodynamic model is used in the CCD formulation for simplicity and computational efficiency.

Authorized licensed use limited to: University of Michigan Library. Downloaded on August 20,2024 at 02:29:56 UTC from IEEE Xplore. Restrictions apply.

This article has been accepted for inclusion in a future issue of this journal. Content is final as presented, with the exception of pagination.

B. Rotor Dynamic Modeling

This study employs a simplified turbine dynamic model that assumes the drivetrain to be rigid and the associated energy loss to be negligible. The rotor dynamics are formulated as follows:

$$I_{\mathrm{HKT}}(c_i)\dot{\omega} = Q - u \tag{1}$$

where ω is the rotor rotating speed, $\dot{\omega}$ is the rotor rotating acceleration, I_{HKT} is the HKT inertia determined by c_i, and u is the generator electromagnetic torque. The rotor drives the generator to rotate. The generator's electromagnetic torque acts as a counterforce that affects the acceleration and, hence, the HKT's rotational speed. We select u as the control variable in this article because its amplitude can be controlled through advanced power electronics and devise-level control systems. Due to the direct-drive configuration, the generator has the same rotational speed as the HKT rotor. Assuming constant generator electrical efficiency, the power (P) from the generator can be characterized as

$$P = u\omega. \tag{2}$$

Assuming constant generator electrical efficiency, we focus on this power for CCD design.

C. Optimizer

CCD involves finding the optimal trajectory to fulfill the dynamic equations shown in (1). This is implemented by imposing defects constraints, calculated by the differences between the dynamic equations and the collocation trajectory at each time spot.

We use SNOPT [36], a sparse sequential quadratic programming package, as the optimizer. The exit condition is set with the optimality and feasibility tolerance below 10^{-6} for all optimizations. The optimization setup and postprocessing are done using pyOptSparse, a common Python interface for constrained optimization [37].

IV. Design Optimization Approaches

To investigate the pros and cons of the CCD approach, we compared HKT optimization using two approaches. One is the conventional sequential design optimization approach used for benchmarking, and the other is CCD. For CCD, we investigate both single-point CCD and multipoint CCD.

A. Sequential Design and Optimization Formulation

The sequential design optimizes the design variables for each discipline in turn [38, Sec. 13.1]. The sequential design process for our example is shown in Fig. 4. The methodology comprises two phases: optimization of the physical design and development of an open-loop optimal control. The physical design optimization maximizes C_P by varying twists θ_i and chords c_i.

The design optimization formulation is defined as

$$\begin{aligned} &\max_{c_i,\theta_i} \ C_P \\ &\text{s.t. } 0.01 \text{ m} \le c_i \le 1 \text{ m}, \ i = 1, 2, \ldots, N \end{aligned}$$

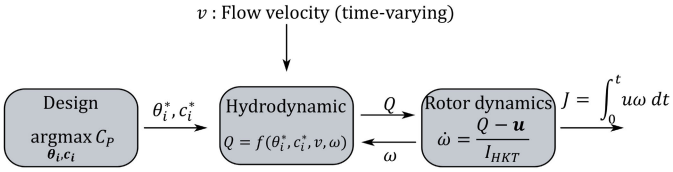

Fig. 4. Illustration of the sequential HKT design-control process. The physical design parameters are decided in the design phase.

$$-30^\circ \le \theta_i \le 30^\circ, \ i = 1, 2, \ldots, N. \tag{3}$$

Once problem (3) is solved, the physical geometry is fixed. In the second step, the optimal control is determined to maximize the electrical energy production for the time period $[0, t]$. The generator efficiency term is assumed to be constant and is neglected in optimizing the control trajectory.

The optimal torque control problem is formulated as

$$\begin{aligned} &\max_{u_{[0,t]}} \ J = \int_0^t u\omega dt \\ &\text{s.t. } \dot{\omega} = \frac{Q-u}{I_{\mathrm{HKT}}} \\ &\quad Q = h\left(\theta_i^*, c_i^*, v, \omega\right) \\ &\quad 0 \le u_{[0,t]} \le u_{\max} \\ &\quad 0 \le \omega \end{aligned} \tag{4}$$

where v is the flow velocity, $u_{\max}$ is the upper bound of the control load, Q is a function of the fixed physical design variables (c_i^* and θ_i^*) and state variables (v and ω), and J is defined to be the total electric power generation according to the model in Section III-B.

As the HKT is designed to rotate in one direction, it is constrained to have a nonnegative rotating speed. We used the third-order Legendre–Gauss–Lobatto collocation to discretize the continuous control trajectory at a set of points equally distributed in time. With such a method, the original co-design problem is converted into a finite-dimensional nonlinear programming problem in Dymos [39], with state and control at each time point treated as design variables. Also, the ordinary differential equations that govern the dynamic models are solved by enforcing nonlinear constraints at each time point.

B. Control Co-Design

CCD represents the application of the MDO that optimizes all disciplines simultaneously to obtain the best possible overall design [38, Sec. 13.1]. As shown in Fig. 5, CCD employs a coupled model consisting of hydrodynamic analysis and rotor dynamics that involve optimal torque control. In this article, two different CCD formulations, single-point CCD and multipoint CCD, are investigated and introduced in Sections IV-B1 and IV-B2.

1) Single-Point CCD: The single-point CCD considers a single time-varying flow profile. The single-point CCD optimization problem is formulated as

$$\begin{aligned} &\max_{c_i,\theta_i,u_{[0,t]}} \ J = \int_0^t u\omega dt \\ &\text{s.t. } \dot{\omega} = \frac{Q-u}{I_{\mathrm{HKT}}} \end{aligned}$$

Authorized licensed use limited to: University of Michigan Library. Downloaded on August 20,2024 at 02:29:56 UTC from IEEE Xplore. Restrictions apply.

This article has been accepted for inclusion in a future issue of this journal. Content is final as presented, with the exception of pagination.

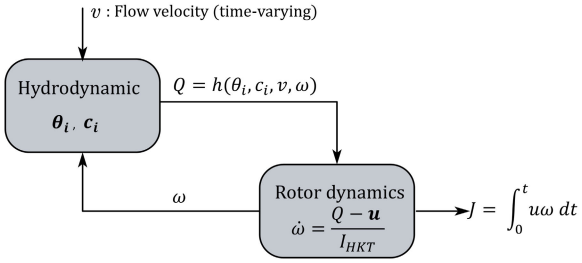

Fig. 5. Illustration of the HKT CCD framework.

$$
\begin{aligned}
&0.01 \text{ m} \le c_i \le 1 \text{ m}, \quad i = 1, 2, \ldots, N \\
&-30^\circ \le \theta_i \le 30^\circ, \quad i = 1, 2, \ldots, N \\
&0 \le u_{[0,t]} \le u_{\max} \\
&0 \le \omega
\end{aligned} \tag{5}
$$

where Q is a nonlinear function of c_i, θ_i, v, and ω. The design problem and the hydrodynamics involved are so complex that convexity or, the lack thereof, cannot be established analytically or numerically. Therefore, we use a physically feasible solution (the Bahaj model) as the initial guess.

2) Multipoint CCD: To yield a more efficient design when average over the year, a multipoint CCD formulation is proposed and implemented. The target is to maximize a weighted sum energy output with a total of M different time-varying flow profiles. The multipoint CCD formulation is given by the following equation:

$$
\begin{aligned}
&\max_{c_i, \theta_i, u_{[0,t]}} \quad J = \sum_{j=1}^{M} f_j \int_0^t u\omega dt \\
&\text{s.t. } \dot{\omega} = \frac{Q - u}{I_{\text{HKT}}} \\
&\quad Q = h(\theta_i, c_i, v, \omega) \\
&\quad 0.01 \text{ m} \le c_i \le 1 \text{ m}, \quad i = 1, 2, \ldots, N \\
&\quad -30^\circ \le \theta_i \le 30^\circ, \quad i = 1, 2, \ldots, N \\
&\quad 0 \le u_{[0,t]} \le u_{\max} \\
&\quad 0 \le \omega
\end{aligned} \tag{6}
$$

where M is the number of the flow profiles investigated, j is the index of the flow profile, and f_j is the corresponding weighting parameter. In this study, the weighting for different flow profiles is decided by the probability distribution of the flow velocity at a given application site. The objective value is an indicator of AEP.

V. Comparisons Between Single-Point CCD and Sequential Method

We first compare CCD and sequential approaches to demonstrate the CCD benefits and when CCD designs outperform their sequential counterparts. We investigated case studies in two scenarios for CCD with or without upper bounds on the control load illustrated. For all the calculations, the initial rotational speed of the turbine is fixed at 6.9 rad/s, which is the steady-state rotational speed of the baseline geometry at its rated speed. The outcomes of the CCD approach are evaluated in comparison to those from sequential designs and a baseline model, ensuring identical constraint and flow conditions for each comparison. We report and discuss the details of the comparison, including the physical designs, optimal control trajectory, HKT rotating speed, and energy production. We consider two scenarios in this study. In the first scenario, we make an assumption that there is no upper bound on the control load, denoted as $u_{\max} = \infty$. The unlimited control authority assumption is impractical. The purpose is to better understand how the physical and control design spaces are coupled. In the second scenario, the upper bound on the control load is $u_{\max} = 700$ Nm, which is within the range of control loads for direct-drive HKT systems with similar rated power.

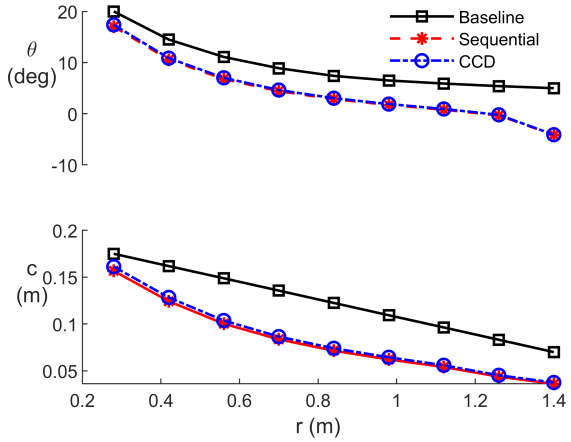

Fig. 6. Comparison between HKT physical design variables optimized with CCD, optimized with the sequential method, and baseline geometry. The upper bound of the control load is assumed to be infinity.

A. Scenario 1: No Constraint on the Control Load

For both CCD and sequential optimization, the scaled HKT model presented in Section II serves as the baseline and initial geometry. We begin by studying the cases with a sinusoidal flow profile $v = 1.5 + 0.2\sin(0.25t)$ m/s. The simulation span is 90 s. The final optimized geometry is shown in Fig. 6. The CCD design exhibits a minor deviation from the sequential method. This is quantified by the relative error in chord lengths, $E_{r,c}$, defined as $E_{r,c} = ((\|c_{\text{seq}} - c_{\text{CCD}}\|_2)/(\|c_{\text{seq}}\|_2))$, be 0.02. Similarly, the relative error in twist angles, $(E_{r,\theta})$, defined as $E_{r,\theta} = ((\|\theta_{\text{seq}} - \theta_{\text{CCD}}\|_2)/(\|\theta_{\text{seq}}\|_2))$, be 0.03. The physical significance can be further explained by examining the λ history shown in Fig. 7. In the scenario without an upper limit on the control load, the optimal torque control strategy successfully identifies control trajectories that consistently maintain the optimal tip speed ratio. Therefore, one can design the physical system first and then optimize the performance through control. The physical design optimization process is decoupled from the control optimization.

The control trajectories resulting from the two design approaches, as shown in Fig. 7, have a great similarity. Transients can be observed at both the beginning and the end of the trajectory. The initial results from the fact that the system has a fixed initial starting velocity. The starting velocity cannot be left as a design variable. This is due to the fact that

Authorized licensed use limited to: University of Michigan Library. Downloaded on August 20,2024 at 02:29:56 UTC from IEEE Xplore. Restrictions apply.

This article has been accepted for inclusion in a future issue of this journal. Content is final as presented, with the exception of pagination.

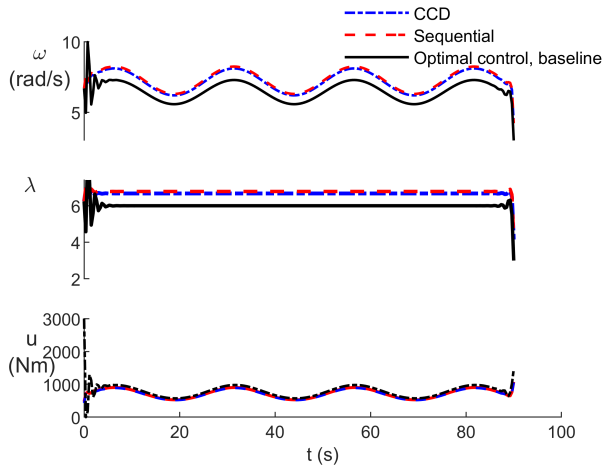

Fig. 7. HKT rotating speed, tip speed ratio, and control load with CCD, sequential design with optimal control, and baseline with optimal control. A sinusoidal flow profile is applied. The upper bound of the control load is assumed to be infinity.

TABLE II

ENERGY PRODUCTION: BASELINE GEOMETRY WITH OPTIMAL TORQUE CONTROL, SEQUENTIAL DESIGN WITH OPTIMAL TORQUE CONTROL, AND CCD. THE UPPER BOUND OF THE CONTROL LOAD IS ASSUMED TO BE INFINITY

Design method	Energy (kJ)	Improvement (%)
Baseline	468.58	0
Sequential	479.55	+2.3
CCD	479.57	+2.3

the initial speed decides the initial kinetic energy stored in the turbine and will always go to the upper bound if left as a design variable. The numerical issue (breaking point) at the end of the simulation is a result of the finite-horizon optimal control approach used in our calculations. The period of interest is set to a fixed duration. The optimization results do not account for power generation beyond the time window, and the trajectory at the end tends to exhibit different characteristics. The generated energy is shown in Table II and compared to that of the baseline design. An improvement of 2.6% in energy production is obtained compared to the baseline. Such improvement comes from the enhancement in the steady-state power coefficient. Fig. 8 shows the C_P values for both the baseline and optimized geometries. The baseline geometry has the maximum C_P of 0.4590 at $\lambda = 5.99$. The optimized geometry obtained with the CCD approaches has $C_P = 0.4718$ at $\lambda = 6.67$. The optimized geometry obtained with the sequential optimization has $C_P = 0.4718$ at $\lambda = 6.78$.

To access the sensitivity of CCD and sequential designs to changes in flow profile, we optimize the designs using a different ramp flow profile: $v = 1.6 - 0.2(0.85)^t$ m/s. Fig. 9 shows the final CCD design using the ramp flow profile converges to a similar geometry as the design optimized with the sinusoidal flow profile. As shown in Fig. 10, the control trajectories are also similar between the sequential design and the CCD design.

When there is no constraint on control load, the optimal torque control is able to maintain optimal λ and peak C_P regardless of the flow profile.

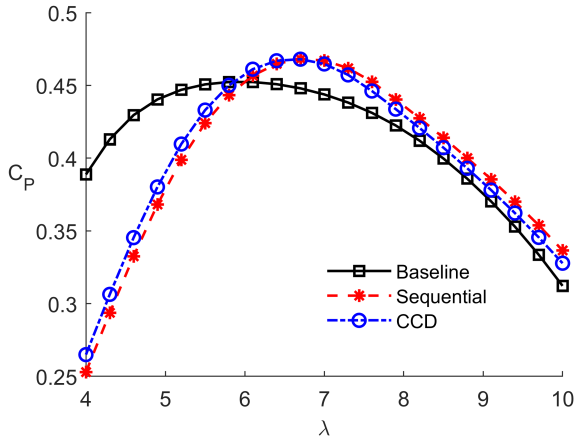

Fig. 8. Comparisons on C_P of physical geometries optimized with CCD, optimized with the sequential method, and baseline geometry. The upper bound of the control load is assumed to be infinity.

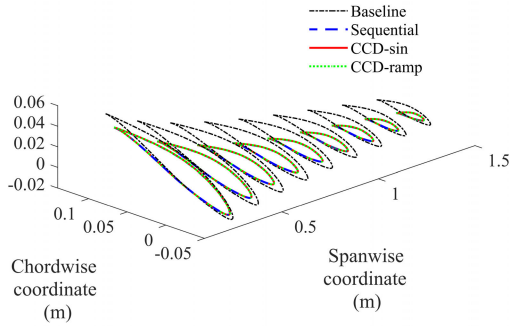

Fig. 9. Comparison between HKT physical geometry optimized with CCD based on a sinusoidal flow profile, optimized with CCD based on a ramp flow profile, optimized with a sequential method, and baseline geometry. No upper bound of the control load is imposed.

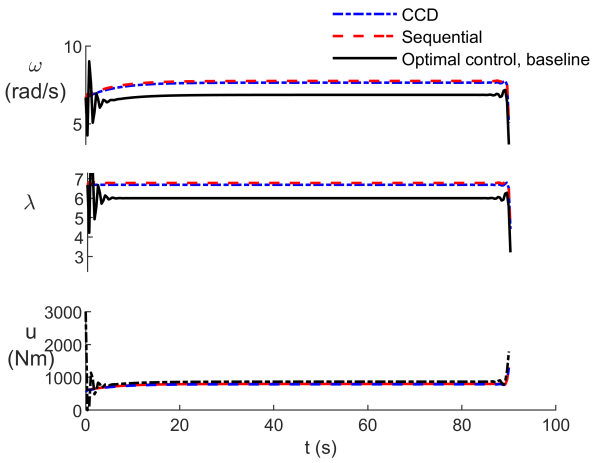

Fig. 10. HKT rotating speed, tip speed ratio, and control load with CCD, sequential design with optimal control, and baseline with optimal control. A ramp flow profile is applied. No upper bound is imposed on the control load.

B. Scenario 2: With a Constraint on the Control Load

Case studies on HKT design optimization are conducted using both the CCD methodology and a sequential approach. These studies impose an upper limit on the control load, set at $u_{\max} = 700$ Nm. The scenarios under examination utilize identical sinusoidal flow profiles as outlined in Scenario 1.

Authorized licensed use limited to: University of Michigan Library. Downloaded on August 20,2024 at 02:29:56 UTC from IEEE Xplore. Restrictions apply.

This article has been accepted for inclusion in a future issue of this journal. Content is final as presented, with the exception of pagination.

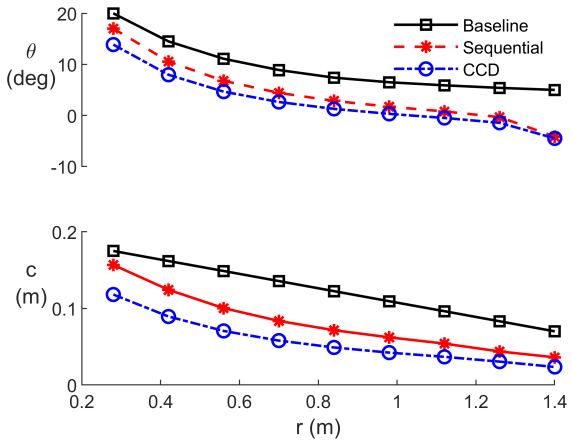

Fig. 11. Comparison between HKT physical design variables optimized with CCD, optimized with the sequential method, and baseline geometry. The upper bound of the control load is 700 Nm.

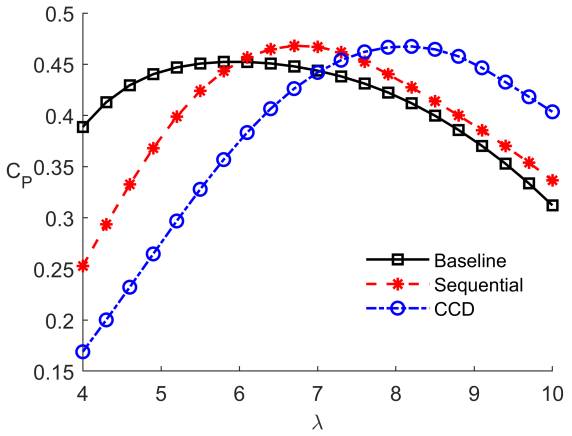

Fig. 12. Comparisons on C_P of physical geometries optimized with CCD, optimized with the sequential method, and baseline geometry. The upper bound of the control load is 700 Nm.

Fig. 11 displays the optimized physical geometries and the corresponding distributions of twist angle and chord length. CCD produces a different physical design than the sequential method. With the flow condition and control constraint described, the CCD design has a shorter chord length and smaller twist angle compared to the sequential approach. As shown in Fig. 12, CCD achieves a maximum power coefficient of 0.4677 at a higher tip speed ratio $\lambda = 8.2$. Because the sequential process does not consider control constraints in physical design optimization, the optimized physical geometry is the same as in Scenario 1.

The HKT rotating speed and control responses of different designs are shown in Fig. 13. Since CCD optimizes the physical geometry variables and control load trajectory simultaneously, the control load constraint affects the physical design. Consequently, the CCD design operates at a higher speed than the sequential design, resulting in a shorter period during which the system operates at the upper bound of the control load. Although the CCD design has a similar maximum C_P to the sequential design, it achieves a 4.8% higher overall energy output than the baseline, higher than the 2.8% improvement achieved by the sequential design (Table III). This difference

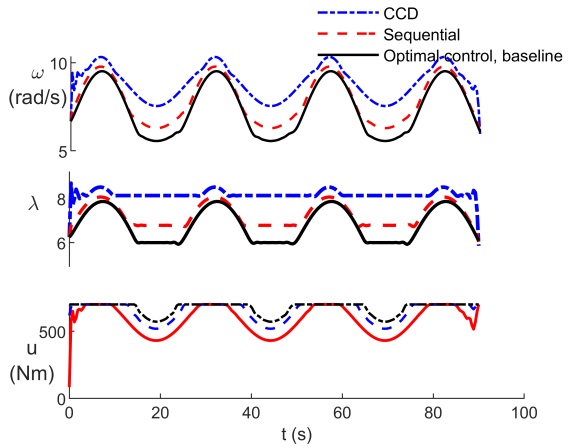

Fig. 13. HKT rotating speed, tip speed ratio, and control load with CCD, sequential design with optimal control, and baseline with optimal control. A sinusoidal flow profile is applied. The upper bound of the control load is 700 Nm.

TABLE III

ENERGY PRODUCTION AND COMPUTATIONAL FOOTPRINT: BASELINE GEOMETRY WITH OPTIMAL TORQUE CONTROL, SEQUENTIAL DESIGN WITH OPTIMAL TORQUE CONTROL, AND CCD. THE UPPER BOUND OF THE CONTROL LOAD IS 700 Nm

Design Method	Energy (kJ)	Improvement (%)	Computation Time (s)
Baseline	454.85	0	191
Sequential	467.65	2.8	446
CCD	476.63	4.8	2948

in physical designs, however, is not observed in the case studies without constraint on control load in Section V-A. The cross-comparisons between the case studies shown in Sections V-A and V-B indicate that the control constraint leads to a coupling between control and design spaces. With this coupling present, CCD finds the optimal design that is not achievable with the sequential method. It is important to note that while CCD expands the search space, its computational footprint is higher than that of the sequential design process. The computational footprint shown in Table III is based on simulations performed on a desktop computer with a 3.4-GHz AMD Ryzen 5950X processor and a serial setup.

Furthermore, different initial guessed values for the physical design variables for the optimizer were tested for both CCD and the sequential design to ensure that the optimization result did not "stuck" at any local optimum. No multiple local minima are observed in the case studied.

The sensitivity of CCD to flow profiles, considering the upper bound of the control load, is investigated with a ramp flow profile: $v = 1.6 - 0.2(0.85)^t$ m/s. Fig. 14 illustrates that CCD designs converge to different geometries based on the flow profiles. The control loads and turbine rotating speed are shown in Fig. 15. Because the control trajectories differ for various flow profiles, the coupling requires adjusting the design space for optimality. Thus, the CCD physical design is sensitive to the flow condition, which leads to practical issues as the physical design cannot change once manufactured. Further investigations are needed for CCD to consider possible flow profiles to produce the final design.

Authorized licensed use limited to: University of Michigan Library. Downloaded on August 20,2024 at 02:29:56 UTC from IEEE Xplore. Restrictions apply.

This article has been accepted for inclusion in a future issue of this journal. Content is final as presented, with the exception of pagination.

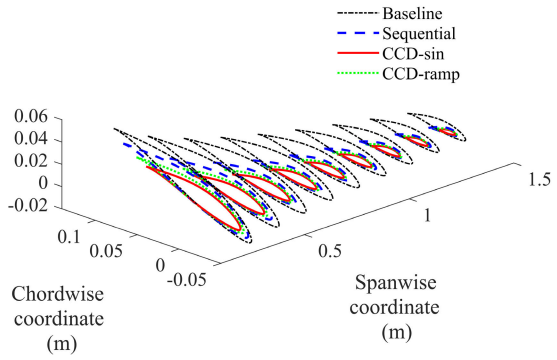

Fig. 14. Comparison between HKT physical geometry optimized with CCD based on a sinusoidal flow profile, optimized with CCD based on a ramp flow profile, optimized with a sequential method, and baseline geometry. The upper bound of the control load is 700 Nm.

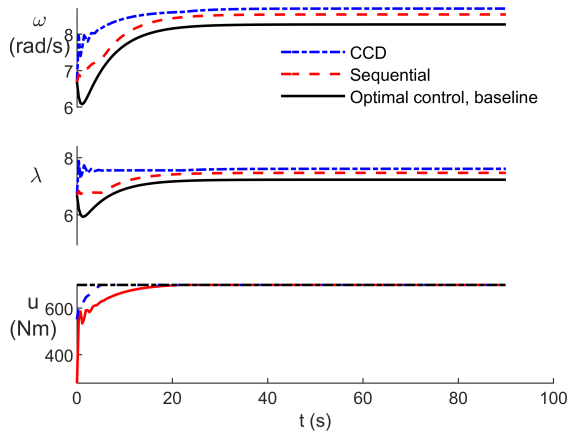

Fig. 15. HKT rotating speed, tip speed ratio, and control load with CCD, sequential design with optimal control, and baseline with optimal control. A ramp flow profile is applied. The upper bound of the control load is 700 Nm.

In the previous examples, we focus on demonstrating the concept and insights. The sinusoidal and ramp inflow profiles simplify the problem setup and reserve the problem characteristics to focus our attention on the findings of the CCD approach comparison. In the following calculations, we look into the design optimization problem through a profile characterized by the flow speed data of the Cape Cod Canal from NOAA [40]. The flow speed data are first approximated with the sum of two sinusoidal functions due to the poor performance of the collocation method with nonsmooth inputs. The results are shown in Fig. 16. Furthermore, the flow speed data are shown for 12 h. The CCD only considers a 3-h duration due to the computation consideration. Due to the symmetry property of the flow profile, one would expect the result to be similar. The geometry design optimization results from the CCD are shown in Fig. 17. With CCD, the optimized turbine generates 5.9 $\times$ 10^7 J of energy, which corresponds to a 5.46-kW power generation. The corresponding control trajectory and ω history are shown in Fig. 18.

VI. Multipoint CCD for AEP Maximization

The result in Section V indicates that the CCD designs optimized with different flow profiles differ from each other with active control constraints. For CCD to yield a single optimal design for different flow profiles, we perform a multipoint AEP maximization. Case studies are conducted using simplified annual probability distributions of flow velocity at a given application site. CCD designs and AEP are then compared.

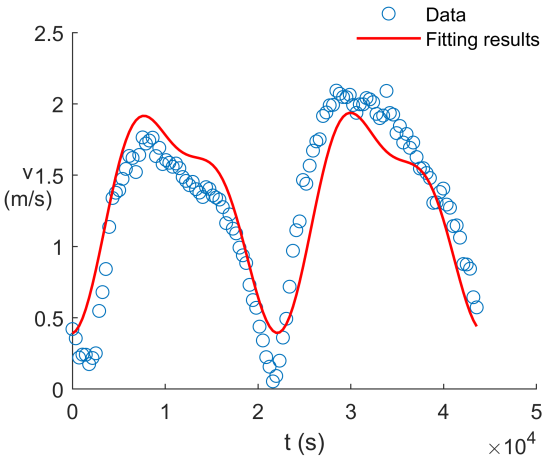

Fig. 16. Flow speed data of the Cape Cod Canal and its fitting result.

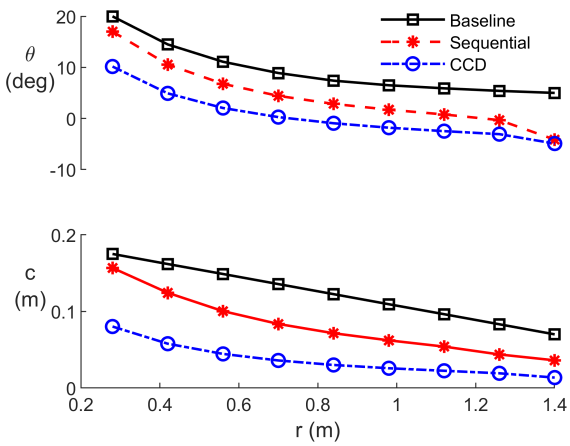

Fig. 17. Comparison between HKT physical design variables optimized with CCD, optimized with the sequential method, and baseline geometry. The flow profile is characterized based on the Cape Cod Canal.

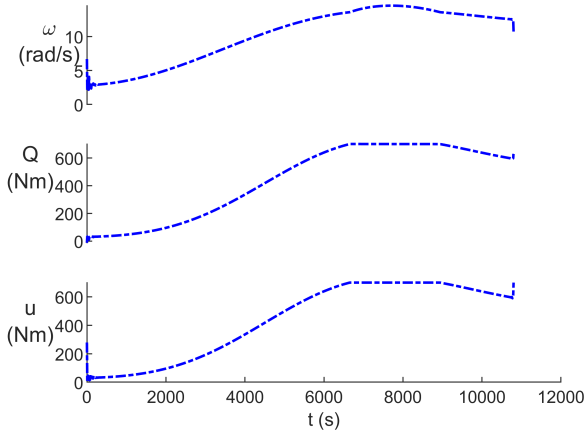

Fig. 18. HKT rotating speed, flow-induced torque, and control load with CCD. Flow profile from the Cape Cop Canal is applied. The upper bound of the control load is 700 Nm.

Authorized licensed use limited to: University of Michigan Library. Downloaded on August 20,2024 at 02:29:56 UTC from IEEE Xplore. Restrictions apply.

This article has been accepted for inclusion in a future issue of this journal. Content is final as presented, with the exception of pagination.

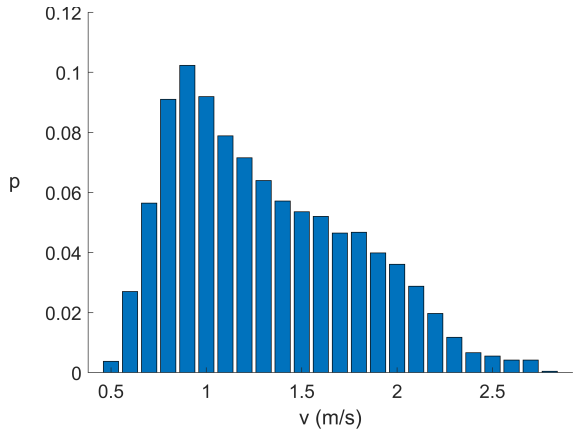

Fig. 19. Annual surface flow speed probability distribution, Mississippi river [41].

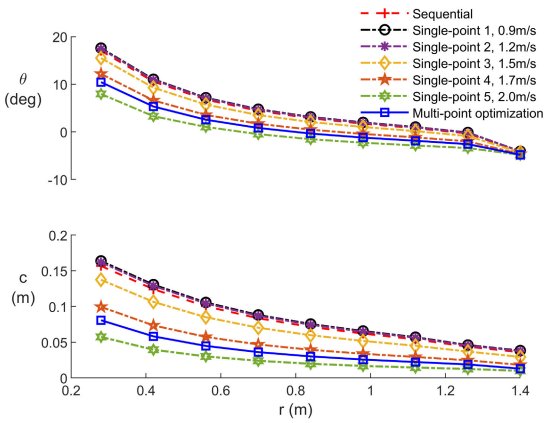

Fig. 20. Comparison between the designs resulted from single-point CCD and multipoint CCD.

TABLE IV
FLOW USED IN MULTIPOINT CCD OPTIMIZATION

Flow velocity (m/s)	Weighting Parameters (–)	Power density (W/m^2)	Weighted power density
0.9	0.33	373	123
1.2	0.23	885	204
1.5	0.17	1,729	298
1.7	0.15	2,518	377
2.0	0.12	4,100	477

A. Comparative Case Studies: Sequential Design, Single-Point CCD, and Multipoint CCD

Comparative case studies are conducted between the sequential design (introduced in Section IV-A), single-point CCD (introduced in Section IV-B1), and multipoint CCD (defined in Section IV-B2) under the same control constraint $u_{\max} = 700$ Nm. After the physical design is decided, control is optimized to maximize the energy output for each flow profile to calculate the annual energy generation with multiple flow conditions. The cases are investigated with a sinusoidal profile, defined as $v = v_a + 0.1\sin(0.1t)$ m/s, for a time span of 120 s. The averaged velocity (v_a) is selected based on the site information. In this study, the HKT is designed with the Mississippi River as a target site. The annual probability distribution of the flow velocity for the site is shown in Fig. 19. Based on probability and power density, we selected flow velocities from 0.9 to 2.1 m/s, with a step size of 0.1 m/s. The weighting parameters (f_j) used in the multipoint CCD calculation are the probability distribution data. Details, including the weighting parameters (probability), power density ($(1/2)\rho v^3$), and weighted power density defined as the production of the probability and power density, are listed in Table IV.

Five single-point optimizations are conducted for five representative profiles with averaged velocities of 0.9, 1.2, 1.5, 1.7, and 2.0 m/s. Among them, the 0.9-m/s flow has the highest probability. The 1.2- and 1.5-m/s flow speed represents a below-rated working region. The 1.7-m/s flow speed represents a rated working region. Also, 2.0-m/s flow represents an over-rated working region. The single-point optimizations are referred to as single-points 1–5 in the rest of this article, corresponding to each row of the flow profiles in Table IV used in the optimization. After the physical design is decided, the AEP is computed using the full velocity probability distribution spectrum. The AEP is calculated as [41]

$$\text{AEP} = \eta \frac{8766}{1000}\frac{1}{2}\rho A \sum_{k=1}^{n} C_p(v_k) v_k^3 p(v_k) \quad \text{[kWh]} \qquad (7)$$

where η is the efficiency (considering availability, drive-train loss, and electrical loss), which is set to 84% [23]. In (7), A is the HKT swept area and $p(v_k)$ is the probability density of the kth flow velocity v_k in the flow speed probability distribution. Due to the limited control authority, C_P cannot maintain a peak value with high inflow velocity and thus is a function of v_k. In this study, the AEP is calculated with an HKT cut-in speed of 0.5 m/s and a cut-out speed of 2.3 m/s. This range covers over 98% of the total distribution.

As shown in Fig. 20, the multipoint CCD results in a physical design different from the one optimized using single-point CCD. Although the 0.9-m/s flow has the highest probability density and, thus, the largest weighting parameter in the optimization, it is shown that the chord length and twist angle distribution from the multipoint CCD is between those optimized with single-point optimizations using 1.7- and 2.0-m/s inflow profiles. Although the two flow profiles have a relatively lower probability, the higher average speed results in a relatively higher weighted power density, contributing more toward energy production. One can also observe that the first two single-point CCD optimizations with relatively slow flow profiles (0.9 and 1.2 m/s) have similar optimized physical design variables. This is because the control constraints are not active. Therefore, these two single-point optimizations converge to the same physical geometry.

Comparisons are also made on AEP, as shown in Table V. For the baseline case, we perform optimal control and compute the sum of the power output with all five flow profiles. The results show that the multipoint CCD optimization leads to the highest weighted energy production among all CCD cases. The multipoint case has 9.47% higher energy production than the baseline physical geometry using open-loop optimal torque control. The multipoint case has 6.95% higher energy production compared with the case when an optimal control

Authorized licensed use limited to: University of Michigan Library. Downloaded on August 20,2024 at 02:29:56 UTC from IEEE Xplore. Restrictions apply.

This article has been accepted for inclusion in a future issue of this journal. Content is final as presented, with the exception of pagination.

TABLE V
COMPARISONS OF AEP BETWEEN SEQUENTIAL, SINGLE-POINT CCD, AND MULTIPOINT CCD

Optimization formulation	**AEP** (kWh)	**Improvement** (%)
Baseline	27,245	–
Sequential	27,932	2.52
Single-point 1	27,745	1.84
Single-point 2	27,776	1.86
Single-point 3	28,442	4.39
Single-point 4	29,446	8.08
Single-point 5	29,615	8.70
Multipoint	29,804	9.47

TABLE VI
DETAILED COMPARISONS ON THE ENERGY PRODUCTION BETWEEN "SINGLE-POINT 5" CCD AND MULTIPOINT CCD

Flow velocity range (m/s)	**Energy output, Single-point 5** (kWh)	**Energy output, Multipoint** (kWh)
0.5–1.1	3,593	3,687
1.2–1.5	6,296	6,465
1.6–1.9	10,331	10,596
2.0–2.3	9,388	9,075

is applied to the HKT designed with the sequential method. Based on the annual energy consumption statistics [42], the average annual electricity consumption per residential customer was 10 791 kWh in 2022. If 100 units of 1.4-m-radius turbine are deployed, the baseline design, sequential design, and CCD design will support 252, 259, and 276 residential customers, respectively. Note that for the sequential design, the effects of the flow speed on the design result from changes in the Reynolds number. Given the assumption listed in Section II-D, the effect is rather minor, and the multipoint sequential design will be identical to the single-point sequential design. The results illustrate the advantage of multipoint CCD in finding the optimal design and equivalently maximizing the AEP that could not be reached with a single-point approach. Another observation is that among the five single-point CCD optimizations, "single-point 5," which uses a 2.0-m/s flow profile in the design optimization, has the second-best energy production. This is because the 2.0-m/s flow has the largest weighted power density, as shown in Table IV. As shown in Table VI, the total energy breakdowns are compared regarding different flow velocity ranges between sequential, multipoint CCD, and "single-point 5."

The multipoint CCD design outperforms the single-point CCD design optimized at the other flow conditions, except at 2.0–2.3-m/s flow velocity, which is around the design point for the single-point CCD. The multipoint design will perform worse than the single-point result designed at that specific condition. However, HKT operates at varying inflow conditions, and hence, the balance between different operating conditions should be considered to achieve the overall optimal performance.

We also compare the torque and rotational speed information of the baseline, the sequential design, and the multipoint CCD. The results are shown in Fig. 21. The multipoint CCD design has a relatively higher rotational speed and reduces the requirements for control load.

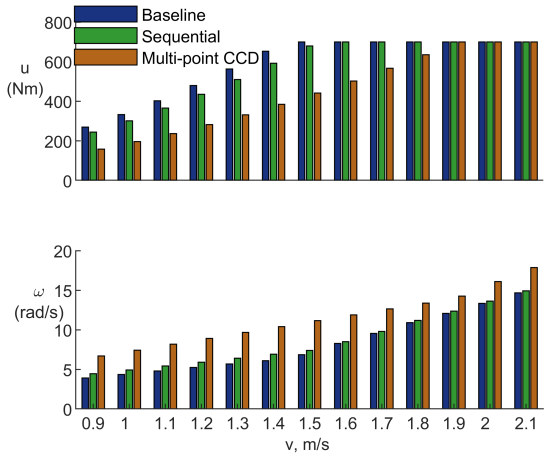

Fig. 21. Torque and rotational speed information of the baseline, the sequential design, and the multipoint CCD.

Despite the fact that the current CCD formulation leads to a different design and a higher AEP value, such a method has its limitations. First, the current collocation method treats the control load at each time spot as a design variable, which significantly increases the complexity of optimization. A computationally efficient strategy is needed to count for a year-long simulation time to further scale the design optimization. Second, the current design formulation has an energy maximization problem as the cost function. This is generally used both in industry and scientific research when the model for cost in maintenance, manufacturing, operation, and deployment is not available. Directly addressing the cost of energy in the optimization with proper capital and operational expenditure models would provide more meaningful insights into the industry. Finally, the work either assumes the flow profile is measured or uses discrete flow speed characterization. Such a method ignores some of the stochastic nature, such as the seasonal characterization. Potential future directions are: 1) to validate the concept with more realistic inflow profiles; 2) to investigate more computationally efficient control parametrization in CCD; and 3) to develop a more robust CCD formulation.

VII. SUMMARY AND CONCLUSION

This article introduces a CCD framework for an HKT rotor design. The CCD framework integrates dynamic and hydrodynamic models and optimizes energy production across various time-varying flow profiles. A thorough comparative analysis was conducted between the CCD approach and the sequential design method to demonstrate the benefits of exploiting the coupling between physical and control spaces through CCD.

The result shows that with no control constraint, there is no coupling between physical variables and control. Under such circumstances, both the sequential design optimization and CCD result in the same design and energy generation. On the other hand, when a control constraint is present, there exists a coupling between physical design and control. Under such circumstances, the CCD leads to improved performance compared to the sequential design method. By comparing CCD results obtained with different flow conditions, we found that the CCD design is sensitive to the flow condition. A multipoint

Authorized licensed use limited to: University of Michigan Library. Downloaded on August 20,2024 at 02:29:56 UTC from IEEE Xplore. Restrictions apply.

This article has been accepted for inclusion in a future issue of this journal. Content is final as presented, with the exception of pagination.

CCD formulated based on a flow probability density distribution was used to maximize AEP. The multipoint CCD design outperforms the single-point design, achieving higher overall energy extraction in terms of AEP. The optimization studies demonstrate that the multipoint CCD strategy is essential for determining the physical design of complex systems such as HKTs that operate in varying flow conditions.

REFERENCES

[1] A. von Jouanne and T. K. A. Brekken, "Ocean and geothermal energy systems," *Proc. IEEE*, vol. 105, no. 11, pp. 2147–2165, Nov. 2017.

[2] A. Hasankhani, Y. Tang, J. VanZwieten, and C. Sultan, "Spatiotemporal optimization for vertical path planning of an ocean current turbine," *IEEE Trans. Control Syst. Technol.*, vol. 31, no. 2, pp. 587–601, Mar. 2023.

[3] P. T. Jacobson, T. M. Ravens, K. W. Cunningham, and G. Scott, "Assssment and mapping of the riverine hydrokinetic resource in the continental United States," Electr. Power Res. Inst., Washington, DC, USA, Tech. Rep. 1026880, 2012.

[4] X. Yang, K. A. Haas, and H. M. Fritz, "Evaluating the potential for energy extraction from turbines in the Gulf stream system," *Renew. Energy*, vol. 72, pp. 12–21, Dec. 2014.

[5] L. E. Myers and A. S. Bahaj, "Experimental analysis of the flow field around horizontal axis tidal turbines by use of scale mesh disk rotor simulators," *Ocean Eng.*, vol. 37, nos. 2–3, pp. 218–227, Feb. 2010.

[6] B.-F. Chen et al., "The deployment of the first tidal energy capture system in Taiwan," *Ocean Eng.*, vol. 155, pp. 261–277, May 2018.

[7] A. P. Thurlbeck and Y. Cao, "Machine learning based condition monitoring for SiC MOSFETs in hydrokinetic turbine systems," in *Proc. IEEE Energy Convers. Congr. Expo. (ECCE)*, Oct. 2022, pp. 1–7.

[8] C. A. Douglas, G. P. Harrison, and J. P. Chick, "Life cycle assessment of the Seagen marine current turbine," in *Proc. Inst. Mech. Eng. M, J. Eng. Maritime Environ.*, vol. 222, no. 1, pp. 1–12, Mar. 2008.

[9] H. Chen, T. Tang, N. Aït-Ahmed, M. E. H. Benbouzid, M. Machmoum, and M. E.-H. Zaïm, "Attraction, challenge and current status of marine current energy," *IEEE Access*, vol. 6, pp. 12665–12685, 2018.

[10] D. Kumar and S. Sarkar, "A review on the technology, performance, design optimization, reliability, techno-economics and environmental impacts of hydrokinetic energy conversion systems," *Renew. Sustain. Energy Rev.*, vol. 58, pp. 796–813, May 2016.

[11] J. Leishman, "Challenges in modeling the unsteady aerodynamics of wind turbines," in *Proc. ASME Wind Energy Symp.*, vol. 7476, Jan. 2002, pp. 141–167.

[12] M. Garcia-Sanz, "Control co-design: An engineering game changer," *Adv. Control Appl., Eng. Ind. Syst.*, vol. 1, no. 1, p. 18, 2019.

[13] D. R. Herber and J. T. Allison, "Nested and simultaneous solution strategies for general combined plant and control design problems," *J. Mech. Des.*, vol. 141, no. 1, Jan. 2019, Art. no. 011402.

[14] J. T. Allison, T. Guo, and Z. Han, "Co-design of an active suspension using simultaneous dynamic optimization," *J. Mech. Des.*, vol. 136, no. 8, Aug. 2014, Art. no. 081003.

[15] A. P. Deshmukh and J. T. Allison, "Multidisciplinary dynamic optimization of horizontal axis wind turbine design," *Struct. Multidisciplinary Optim.*, vol. 53, no. 1, pp. 15–27, Jan. 2016.

[16] L. Y. Pao et al., "Control co-design of 13 MW downwind two-bladed rotors to achieve 25% reduction in levelized cost of wind energy," *Annu. Rev. Control*, vol. 51, pp. 331–343, Jan. 2021.

[17] K. Naik, S. Beknalkar, J. Reed, A. Mazzoleni, H. Fathy, and C. Vermillion, "Pareto optimal and dual-objective geometric and structural design of an underwater kite for closed-loop flight performance," *J. Dyn. Syst., Meas., Control*, vol. 145, no. 1, Jan. 2023, Art. no. 011005.

[18] R. G. Coe, G. Bacelli, S. Olson, V. S. Neary, and M. B. R. Topper, "Initial conceptual demonstration of control co-design for WEC optimization," *J. Ocean Eng. Mar. Energy*, vol. 6, no. 4, pp. 441–449, Nov. 2020.

[19] A. C. M. O'Sullivan and G. Lightbody, "Co-design of a wave energy converter using constrained predictive control," *Renew. Energy*, vol. 102, pp. 142–156, Mar. 2017.

[20] S. Toumi, E. Elbouchikhi, Y. Amirat, M. Benbouzid, and G. Feld, "Magnet failure-resilient control of a direct-drive tidal turbine," *Ocean Eng.*, vol. 187, Sep. 2019, Art. no. 106207.

[21] B. Jiang, M. R. Amini, Y. Liao, J. R. R. A. Martins, and J. Sun, "Control co-design of a hydrokinetic turbine with open-loop optimal control," in *Proc. Int. Conf. Offshore Mech. Arctic Eng.*, vol. 85932. New York, NY, USA: American Society of Mechanical Engineers, 2022, Art. no. V008T09A006.

[22] A. S. Bahaj, A. F. Molland, J. R. Chaplin, and W. M. J. Batten, "Power and thrust measurements of marine current turbines under various hydrodynamic flow conditions in a cavitation tunnel and a towing tank," *Renew. Energy*, vol. 32, no. 3, pp. 407–426, Mar. 2007.

[23] M. Garcia-Sanz, "Engineering microgrids with control co-design: Principles, methods, and metrics," *IEEE Electrific. Mag.*, vol. 9, no. 3, pp. 8–17, Sep. 2021.

[24] K.-H. Kim, T. L. Van, D.-C. Lee, S.-H. Song, and E.-H. Kim, "Maximum output power tracking control in variable-speed wind turbine systems considering rotor inertial power," *IEEE Trans. Ind. Electron.*, vol. 60, no. 8, pp. 3207–3217, Aug. 2013.

[25] M. R. Amini, B. Jiang, Y. Liao, K. Naik, J. R. R. A. Martins, and J. Sun, "Control co-design of a hydrokinetic turbine: A comparative study of open-loop optimal control and feedback control," in *Proc. Amer. Control Conf. (ACC)*, May 2023, pp. 3728–3734.

[26] A. P. Deshmukh, D. R. Herber, and J. T. Allison, "Bridging the gap between open-loop and closed-loop control in co-design: A framework for complete optimal plant and control architecture design," in *Proc. Amer. Control Conf. (ACC)*, Jul. 2015, pp. 4916–4922.

[27] E. Chica, F. Perez, A. Rubio-Clemente, and S. Agudelo, "Design of a hydrokinetic turbine," in *WIT Transactions on Ecology and the Environment*, vol. 195. Southampton, U.K.: WIT Press, 2015, pp. 137–148.

[28] R. W. Deters, G. K. A. Krishnan, and M. S. Selig, "Reynolds number effects on the performance of small-scale propellers," in *Proc. 32nd AIAA Appl. Aerodyn. Conf.*, Jun. 2014, p. 2151.

[29] F. Alimenti et al., "Noncontact measurement of river surface velocity and discharge estimation with a low-cost Doppler radar sensor," *IEEE Trans. Geosci. Remote Sens.*, vol. 58, no. 7, pp. 5195–5207, Jul. 2020.

[30] S. A. Ning, "A simple solution method for the blade element momentum equations with guaranteed convergence," *Wind Energy*, vol. 17, no. 9, pp. 1327–1345, Sep. 2014.

[31] J. S. Gray, J. T. Hwang, J. R. R. A. Martins, K. T. Moore, and B. A. Naylor, "OpenMDAO: An open-source framework for multidisciplinary design, analysis, and optimization," *Struct. Multidisciplinary Optim.*, vol. 59, no. 4, pp. 1075–1104, Apr. 2019.

[32] A. Ning, "Using blade element momentum methods with gradient-based design optimization," *Struct. Multidisciplinary Optim.*, vol. 64, no. 2, pp. 991–1014, Aug. 2021.

[33] M. Drela, "XFOIL: An analysis and design system for low Reynolds number airfoils," in *Proc. Int. Conf. Low Reynolds Number Aerodyn.*, Notre Dame, IA, USA. Berlin, Germany: Springer, Jun. 1989, pp. 1–12.

[34] L. C. Henriksen, M. H. Hansen, and N. K. Poulsen, "A simplified dynamic inflow model and its effect on the performance of free mean wind speed estimation," *Wind Energy*, vol. 16, no. 8, pp. 1213–1224, Nov. 2013.

[35] O. Apata and D. T. O. Oyedokun, "An overview of control techniques for wind turbine systems," *Sci. Afr.*, vol. 10, Nov. 2020, Art. no. e00566.

[36] P. E. Gill, W. Murray, and M. A. Saunders, "SNOPT: An SQP algorithm for large-scale constrained optimization," *SIAM Rev.*, vol. 47, no. 1, pp. 99–131, Jan. 2005.

[37] E. Wu, G. Kenway, C. A. Mader, J. Jasa, and J. R. R. A. Martins, "pyOptSparse: A Python framework for large-scale constrained nonlinear optimization of sparse systems," *J. Open Source Softw.*, vol. 5, no. 54, p. 2564, Oct. 2020.

[38] J. R. R. A. Martins and A. Ning, *Engineering Design Optimization*. Cambridge, U.K.: Cambridge Univ. Press, 2021. [Online]. Available: https://mdobook.github.io

[39] R. Falck, J. S. Gray, K. Ponnapalli, and T. Wright, "Dymos: A Python package for optimal control of multidisciplinary systems," *J. Open Source Softw.*, vol. 6, no. 59, p. 2809, Mar. 2021.

[40] National Oceanic and Atmospheric Administration. (2024). *NOAA Tides and currents—Current Data*. [Online]. Available: https://tidesandcurrents.noaa.gov/currents_info.html

[41] V. S. Neary et al., "Methodology for design and economic analysis of marine energy conversion (mec) technologies," Water Power Technol. Dept., Sandia Nat. Laboratories, Albuquerque, NM, USA, Tech. Rep. SAND2014-9040, 2014.

[42] U.S. Energy Information Administration. (2022). *How Much Electricity Does an American Home Use?* Accessed: Jun. 28, 2024. [Online]. Available: https://www.eia.gov/tools/faqs/faq.php?id=97&t=3

Authorized licensed use limited to: University of Michigan Library. Downloaded on August 20,2024 at 02:29:56 UTC from IEEE Xplore. Restrictions apply.

This article has been accepted for inclusion in a future issue of this journal. Content is final as presented, with the exception of pagination.

Boxi Jiang received the B.S. degree in mechanical engineering from Shandong University, Jinan, Shandong, China, in 2018, and the M.S. degree in mechanical engineering from Virginia Tech, Blacksburg, VA, USA, in 2020. He is currently pursuing the Ph.D. degree with the Department of Naval Architecture and Marine Engineering, University of Michigan, Ann Arbor, MI, USA.

His research is on the control and control co-design for hydrokinetic turbines.

Mohammad Reza Amini received the Ph.D. degree in mechanical engineering from Michigan Technological University, Houghton, MI, USA, in 2017.

He is currently a Research Scientist at the College of Engineering, University of Michigan, Ann Arbor, MI, USA, focusing on nonlinear, adaptive, robust, and predictive control theories for intelligent transportation, automotive, and energy systems.

Yingqian Liao received the Ph.D. degree from the University of Michigan, Ann Arbor, MI, USA, in 2021.

She is currently a Post-Doctoral Researcher at the National Renewable Energy Laboratory, Golden, CO, USA. The work presented in this article was conducted during her time as a Post-Doctoral Research Fellow at the University of Michigan. Her research interests include multidisciplinary design optimization, hydrodynamics, fluid–structure interaction, and composite structures.

Kartik Naik received the Ph.D. degree in aerospace engineering from North Carolina State University, Raleigh, NC, USA, in 2022.

He is currently a Research Faculty Member at the University of Michigan, Ann Arbor, MI, USA, specializing in co-optimization and control design for energy systems. His research interests include state-of-health estimation and predictive maintenance, real-time control implementation on hardware, and exploring tech-to-market pathways for emerging technologies.

Joaquim R. R. A. Martins received the Ph.D. degree from Stanford University, Stanford, CA, USA, in 2002.

He is currently a Professor of aerospace engineering at the University of Michigan, Ann Arbor, MI, USA. His research involves the development and application of multidisciplinary design optimization (MDO) methodologies to the design of aircraft configurations, with a focus on high-fidelity simulations that take advantage of high-performance parallel computing.

Dr. Martins is a fellow of American Institute of Aeronautics and Astronautics and the Royal Aeronautical Society.

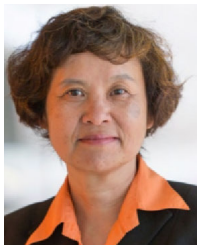

Jing Sun (Fellow, IEEE) received the Ph.D. degree from the University of Southern California, Los Angeles, CA, USA, in 1989.

She is currently a Professor with the Naval Architecture and Marine Engineering Department, University of Michigan, Ann Arbor, MI, USA. Her research interests include modeling, control, and optimization of dynamic systems, with applications to marine and automotive systems.

Dr. Sun is a fellow of the National Academy of Inventors, IFAC, and the Society of Naval Architects and Marine Engineers. She was a recipient of the 2003 IEEE Control System Technology Award.

Authorized licensed use limited to: University of Michigan Library. Downloaded on August 20,2024 at 02:29:56 UTC from IEEE Xplore. Restrictions apply.